

Orbital-angular-momentum-enhanced phase estimation using non-Gaussian states with photon lossYong-Jian Chen ¹, Jin-Wei Gao ^{2,*}, Jin-Xuan Han,¹ Zhong-Hui Yuan,¹ Ruo-Qi Li ¹,
Yong-Yuan Jiang,^{1,3,4,5} and Jie Song ^{1,3,4,5,†}¹*School of Physics, Harbin Institute of Technology, Harbin 150001, China*²*School of Electronic Information Engineering, China West Normal University, Nanchong 637002, Sichuan, China*³*Key Laboratory of Micro-Nano Optoelectronic Information System, Ministry of Industry and Information Technology, Harbin 150001, China*⁴*Key Laboratory of Micro-Optics and Photonic Technology of Heilongjiang Province, Harbin Institute of Technology, Harbin 150001, China*⁵*Collaborative Innovation Center of Extreme Optics, Shanxi University, Taiyuan, Shanxi 030006, China*

(Received 10 March 2023; revised 2 July 2023; accepted 28 July 2023; published 22 August 2023)

This study investigates the use of orbital angular momentum (OAM) to enhance phase estimation in Mach-Zehnder interferometers by employing non-Gaussian states as input resources in the presence of noise. Our research demonstrates that non-Gaussian states, particularly the photon-subtraction-then-addition state, exhibit the best sensitivity in the presence of symmetric noise. Additionally, a higher order of the Bose operator of non-Gaussian states provides better sensitivity for symmetric noise. OAM can mitigate the deterioration of noise, making it possible to estimate small phase shifts $\theta \rightarrow 0$. OAM enhances the resolution and sensitivity of all input states and mitigates the deterioration caused by photon loss. Additionally, OAM enhances the resolution and sensitivity of all input states, enabling the sensitivity to approach the $1/N$ limit even under significant photon loss (e.g., 50% symmetric photon loss). These results hold promise for enhancing the sensitivity and robustness of quantum metrology, particularly in the presence of significant photon loss.

DOI: [10.1103/PhysRevA.108.022613](https://doi.org/10.1103/PhysRevA.108.022613)**I. INTRODUCTION**

Interferometric phase estimation is a critical research topic in various growing fields, such as gravitational wave detection [1] and quantum-enhanced dark-matter searches [2]. Among optical interferometers, the Mach-Zehnder interferometer (MZI) is a widely used and practical tool for estimating small phase changes [3–9]. Improving the sensitivity of phase estimation in the MZI has been the focus of extensive research in recent years [10–16]. Many efforts have been made to find better input-state candidates to improve the resolution and sensitivity. With a classical light field as an input resource for the MZI, sensitivity can reach only the shot-noise limit (SNL). However, nonclassical states of light provide numerous potential choices for quantum metrology. The Heisenberg limit (HL) is theoretically attainable with the use of a nonclassical light state [17]. The two-mode squeezed vacuum state (TMSV) with a parity measurement beats the HL while saturating the quantum Cramér-Rao Bound (QCRB) [18].

Non-Gaussian states [19–24], which have emerged as promising candidates, offer the potential to enhance quantum metrology [25–28]. A variety of nonclassical states, including photon-subtracted and photon-added states [29,30], as well as coherent, squeezed vacuum states and NOON-like

states [31–33], have been studied to improve phase estimation. From a practical standpoint, the impact of noise [34–37], particularly photon-loss-induced decoherence, poses a significant challenge in the pursuit of enhanced sensitivity and resolution [38,39]. Both theoretical and experimental studies have indicated that orbital angular momentum (OAM) offers a degree of resilience to light beams in noisy environments [40–42]. As such, the exploration of non-Gaussian states and OAM has become an important area of study. These techniques harbor the potential to facilitate precise phase estimation and heightened sensitivity

Our investigation highlights the potential of utilizing OAM to increase the sensitivity of phase estimation in the MZI system by employing non-Gaussian states as input states. We use a balanced (50:50) beam-splitter MZI and parity detection as the optimal setup [14,15,31,43]. The results of our research reveal that non-Gaussian states display superior sensitivity compared to the TMSV state under symmetric and weakly symmetric noise. To further enhance sensitivity in the presence of photon loss for a specific non-Gaussian state, we employ the lower order of the Bose operator and implement balanced photon loss. OAM effectively mitigates noise degradation, facilitating small-phase-shift estimation. Furthermore, OAM enhances the resolution and sensitivity of all input states while counteracting the negative impact of photon loss and enables sensitivity to approach the $1/N$ limit even under significant photon loss, such as 50% symmetric photon loss. We also analyze the statistical properties of quantum states in the MZI system by von Neumann entropy and the Wigner

*jwgao@cwnu.edu.cn

†jsong@hit.edu.cn

function [44–47]. Therefore, this work provides prospects for realizing higher sensitivity in quantum metrology with the presence of significant noise.

II. PHASE-ESTIMATION PROTOCOL ENHANCED BY NON-GAUSSIAN STATES and OAM

A. The design of the MZI system and the expression of non-Gaussian states

Using non-Gaussian states is a feasible method to find better input-state candidates [17,48–50]. Exploring photon subtraction (PS), photon addition (PA), and their superposition state as the input resource provides a good example [51–53]. We write the expression of such states by harnessing the Bose operator on the TMSV state, represented by $\hat{a}(\hat{a}^\dagger)|\Psi\rangle_{\text{TMSV}}$. Here, we introduce a kind of non-Gaussian state determined by different sequences and orders of Bose operators as

$$\begin{aligned} |\hat{\Psi}\rangle_{\text{PA}} &= N_p \hat{a}^{\dagger G} \hat{b}^{\dagger H} \hat{S}(\xi)|0, 0\rangle, \\ |\hat{\Psi}\rangle_{\text{PS}} &= N_p \hat{a}^J \hat{b}^K \hat{S}(\xi)|0, 0\rangle, \\ |\hat{\Psi}\rangle_{\text{PAS}} &= N_p \hat{a}^{\dagger G} \hat{b}^{\dagger H} \hat{a}^J \hat{b}^K \hat{S}(\xi)|0, 0\rangle, \\ |\hat{\Psi}\rangle_{\text{PSA}} &= N_p \hat{a}^{\dagger G} \hat{b}^{\dagger H} \hat{a}^J \hat{b}^K \hat{S}(\xi)|0, 0\rangle, \end{aligned} \quad (1)$$

where N_p denotes a normalized parameter; $\hat{S}(\xi)$ represents the two-mode squeezing operator; $\xi = re^{i\psi}$, where r is the squeezing parameter and ψ is the squeezing angle; and $\hat{a}(\hat{a}^\dagger)$ and $\hat{b}(\hat{b}^\dagger)$ serve as annihilation (creation) operators for modes a and b , respectively. Equation (1) provides the formulation for the PA, PS, photon-addition-then-subtraction (PAS), and photon-subtraction-then-addition (PSA) states. It should be noted that G and H symbolize the order of the Bose operators, as discussed in previous works [54,55]. Non-Gaussian states in which $G = H$ exhibit superior sensitivity compared to those in which $G \neq H$. Consequently, our discussion is focused primarily on the precondition of $G = H$. For $G = H = 1$, we label the non-Gaussian states as PA11, PS11, PAS11, and PSA11. When $G = H = 2$, these states are referred to as PA22, PS22, PAS22, and PSA22. The appended numbers in each case correspond to the values of G and H .

Figure 1 explicitly shows the phase-estimation protocol. Two 50:50 beam splitters (BSs) and two phase shifters compose the main structure of the MZI. The two BSs are represented by the operators $U_{\text{BS}_1} = \exp[-i\frac{\pi}{4}(\hat{a}^\dagger \hat{b} + \hat{a} \hat{b}^\dagger)]$ and $U_{\text{BS}_2} = \exp[i\frac{\pi}{4}(\hat{a}^\dagger \hat{b} + \hat{a} \hat{b}^\dagger)]$, respectively. Dove prisms (DPs) embedded in modes c and d are phase shifters denoted by $\exp(-i\theta \hat{n})$, where \hat{n} is the photon number operator and θ represents the phase-shift angle. The protocol proposes two opposite phase shifts $\frac{\theta}{2}$ in modes c and d . To investigate the photon loss, we insert two more BSs with transmittance $T_{a(b)}$ between BS_1 and BS_2 to generate photon loss.

The OAM beam is characterized by a light beam that exhibits a helical phase structure within its wave front, with each photon carrying an OAM value of $L\hbar$, where L signifies the azimuthal angular parameter, also known as the topological charge of the OAM beam. As the value of L increases, both the radius of the beam's cross-sectional area and the angle between the beam's Poynting vector and the optical axis increase. The topological charge L (i.e., $L, 2L, 3L, \dots$) serves to enhance the parity measurement results and sensitivity [refer

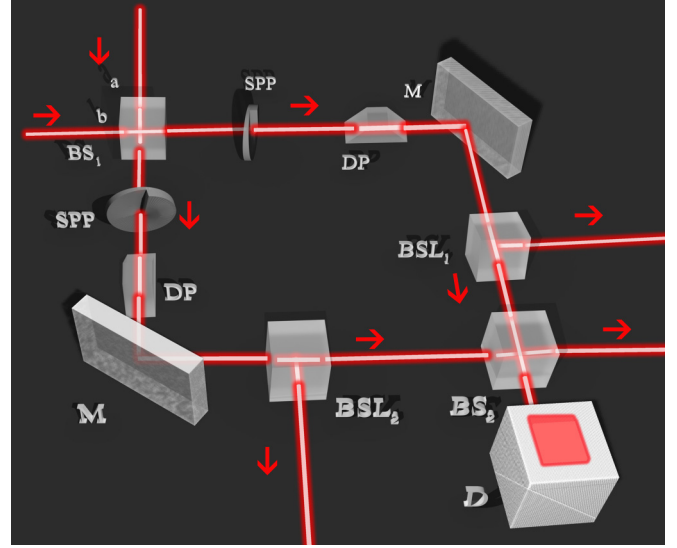


FIG. 1. Schematic of the Mach-Zehnder interferometer system. Fed by quantum states input from ports a and b , the light is transmitted through paths c and d and finally detected in port e or f with the detector (D). After a phase shift generated by a Dove prism (DP), we use two arbitrary-rate beam splitters to simulate the photon loss (BSL). Spiral phase plates (SPP) are used to bring OAM. The mirror (M) can change the direction of the light field.

to Eqs. (5), (B9), and (B11) for further details]. In this study, we modulate the beam's phase [e.g., using spiral phase plates (SPPs)], directly imparting a helical phase onto the beam to generate an OAM beam. The OAM in the input state can act as a “gear” to magnify the phase-shift term, thereby enabling the estimation of small phase shifts [56–60].

The light-detection scheme at the output mode(s) of the MZI determines the best sensitivity we can obtain. Among many detection approaches, the parity measurement can exploit the potential of nonclassical light and reach the QCRB [14,15,61] (for details see Appendix A). This work uses a parity operator in one of the output modes, represented by $\Pi_b = (-1)^{\hat{b}^\dagger \hat{b}}$. The expectation value of the measurement signal can be represented by

$$\langle \Pi_b \rangle = \text{Tr}[\rho_{\text{out}} \Pi_b], \quad (2)$$

where ρ_{out} denotes the density matrix of the output state.

As an example, we give the expression for the parity signal derived by Eq. (2) using PSA11 as the input state,

$$\begin{aligned} \langle \Pi \rangle_{\text{PSA11}(\theta+\pi/2)} &= ((1-z^2)\{-4z^2(2-63z^4+39z^8 \\ &+ 14z^{12})\cos L(\pi+2\theta) + z^4[-4 \\ &+ 315z^4 - 252z^8 + 8z^{12} + 4*(15 \\ &- 41z^4 + 9z^8)\cos 2L(\pi+2\theta) + 4z^2 \\ &\times (-9+z^4)\cos 3L(\pi+2\theta) + z^4 \\ &\times \cos 4L(\pi+2\theta)\})\}) / \{8(1+z^4+2z^2 \\ &\times \cos 2L\theta)^{\frac{1}{2}}[1+z^4+2z^2\cos L(\pi+2\theta)]\}, \end{aligned} \quad (3)$$

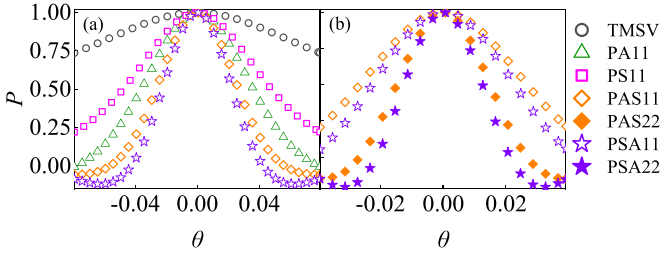


FIG. 2. Normalized detection signal P as a function of phase shift θ for all input states with squeezing parameter $r = 1.096$. The black circles denote the TMSV state. As for the non-Gaussian states, we use PA, PS, PAS, and PSA (triangles, squares, diamonds, and stars). We use open symbols to represent $G = H = 1$ and solid symbols for $G = H = 2$.

where z denotes $\tanh(r)$ and θ is the phase shift. The details of the calculation and the results for other input states are shown in Appendix B. As shown in Eq. (5), there are three parameters that determine $\langle \Pi \rangle$: the squeezing parameter r , phase shift θ , and OAM quantum number L .

B. The enhancement caused by the non-Gaussian state and OAM

Figure 2 shows the signal of the parity detection $\langle \Pi \rangle$ as a function of the phase shift θ , where the label P is used to represent $\langle \Pi \rangle$. The full width at half maximum (FWHM) of the signal curve is one of the universal criteria for determining the resolution. For a narrower signal peak, a small phase shift leads to a distinct change in the P value, indicating a higher resolution. It is apparent from Fig. 2(a) that for the same squeezing parameter, the TMSV has the worst resolution and PSA11 has the best resolution. Figure 2(b) demonstrates that the higher-order Bose operator leads to superior resolution.

There are only two outcomes for parity detection: $+$ for even and $-$ for odd. According to Ref. [62], the classical Fisher information F_C determined by θ can be used to calculate the detection sensitivity, represented by Eq. (4),

$$\Delta\theta = \frac{1}{\sqrt{F_C}} = \frac{\sqrt{1 - \langle \Pi_b \rangle}}{|\partial \langle \Pi_b \rangle / \partial \theta|}. \tag{4}$$

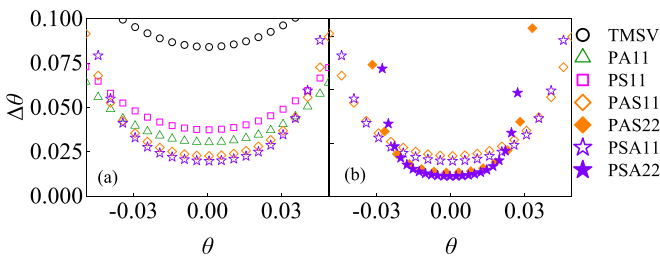


FIG. 3. Phase-estimation sensitivity $\Delta\theta$ as a function of the phase shift θ with squeezing parameter $r = 1.096$ for all input states. (a) shows the states with $G = H = 1$. In (b), we depict the PAS and PSA states with different orders of the Bose operator. We use open symbols to denote input states with $G = H = 1$ and solid symbols for $G = H = 2$.

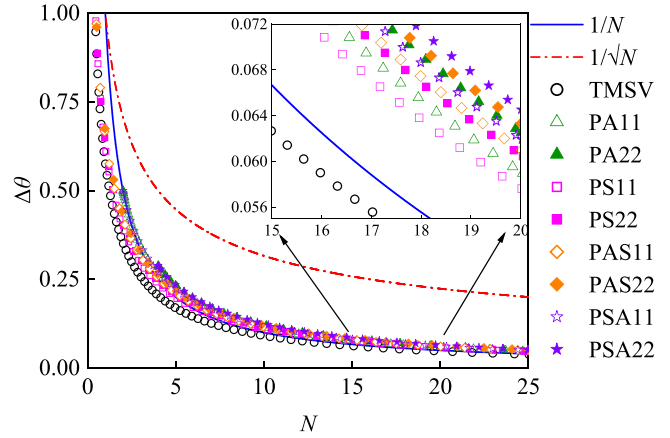


FIG. 4. Sensitivity $\delta\theta$ as a function of mean photon number N with no photon loss. The phase shift has been taken as $\theta = 10^{-4}$. The open (solid) symbols represent the state with $G = H = 1$ ($G = H = 2$).

To investigate how phase sensitivity changes as a function of θ , we plot Fig. 3 using Eq. (4). We can see that in the case of $\theta \rightarrow 0$, the lowest bound of the phase sensitivity is obtained [62,63]. The data in Fig. 3(a) suggest that the TMSV state has the worst sensitivity and the PSA11 state has the best sensitivity. Figure 3(b) implies that the higher-order Bose operator leads to a lower $\Delta\theta$ bound. Overall, these results show that with a fixed squeezing parameter r , the PSA state has the best resolution and sensitivity for a small phase shift of 10^{-3} . Also, with the increase of G and H , both resolution and sensitivity increase.

On the other hand, we study the sensitivity of the input state as a function of the mean photon number N in Fig. 4. As we can see from Fig. 4, with a fixed mean photon number, the TMSV state exhibits better sensitivity than non-Gaussian states when there is no photon loss.

In Fig. 5 we visualize the enhancement of the resolution caused by OAM. Figure 5 depicts the normalized detection signal P as a function of θ for various topological charges L . We use the signal's FWHM (denoted by the label F) as the criterion to compare the resolutions. From Fig. 5(a), the results demonstrate that the higher OAM provides superior resolution. We plot F versus OAM number L in Fig. 5(b) for $r = 0.2, 0.4$, and 0.8 . The enhancement caused by OAM is prominent, which will lead to higher resolution and sensitivity.

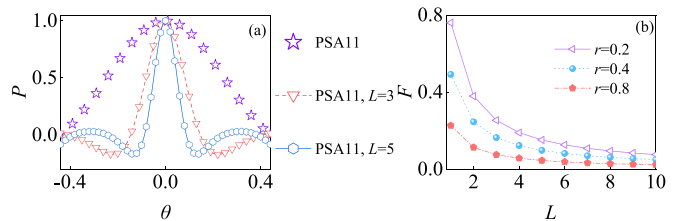


FIG. 5. (a) Detection signal P as a function of phase shift for the PSA11 input state with $r = 1.096$. Stars, triangles, and hexagons represent the PSA11 state with no OAM added, $L = 3$, and $L = 5$, respectively. (b) FWHM of the PSA11 state varies with L for $r = 0.2, 0.4$, and 0.8 .

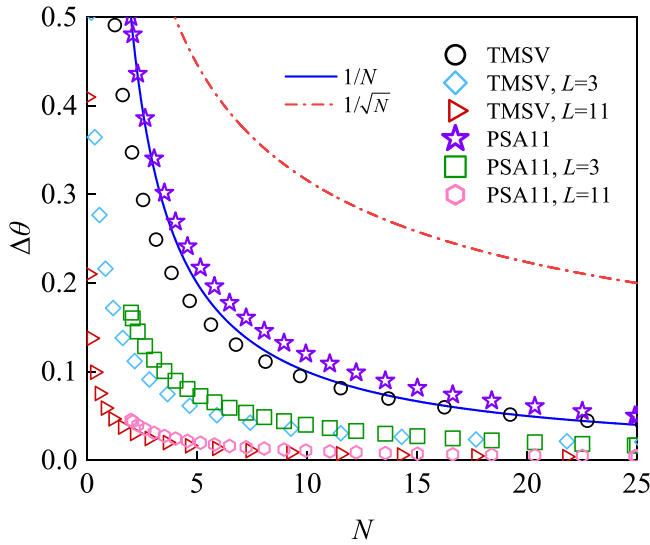


FIG. 6. Phase-estimation sensitivity $\Delta\theta$ as a function of the mean photon number N without noise for no OAM-added, $L = 3$, and $L = 11$. The solid blue line and red dash-dotted lines represent the $1/N$ and $1/\sqrt{N}$ limits. Stars, squares, and hexagons represent the sensitivity of the PSA11 state with no OAM enhancement, $L = 3$, and $L = 11$. Circles, diamonds, and triangles indicate the TMSV state with no OAM enhancement, $L = 3$, and $L = 11$, respectively. The phase shift is fixed at $\theta = 10^{-4}$.

We plot the OAM-enhanced sensitivity $\Delta\theta$ against the mean photon number N in Fig. 6, where the phase shift is fixed at $\theta = 10^{-3}$. Figure 6 uses the TMSV and PSA11 states as examples to demonstrate $\Delta\theta$ versus N for no OAM added, $L = 3$, and $L = 11$. Without photon loss, the TMSV state has better sensitivity than non-Gaussian states. Sensitivity improves with increasing L .

III. THE EFFECT OF VARIOUS NOISES AND THEIR MITIGATION

A. The influence of symmetric and asymmetric noises

Unavoidable photon loss leads to a worse $\Delta\theta$. In the protocol, a BS is used to cause photon loss in both arms of MZI. We define $T_a = T_b = T$ as symmetric noise and $T_a \neq T_b$ as asymmetric noise. Weakly symmetric noise is defined as $T_b - T_a \leq 0.4$, and strongly symmetric noise is defined as $T_b - T_a \geq 0.4$. We investigate how the noise influences the phase estimation. We plot $\Delta\theta$ as a function of θ with various noises for all input states in Fig. 7, where we set the squeezing parameter as $r = 1.096$. Figure 7 reveals that the lowest bound of $\Delta\theta$ for non-Gaussian states gets worse with the increase of $T_b - T_a$, as is evident from Figs. 7(e) to 7(a). The results demonstrate that in order to further improve the sensitivity, balancing the photon loss for non-Gaussian states is an effective way. The PSA state exhibits the best sensitivity for small phase shifts in the presence of symmetric noise, while higher-order Bose operators provide even greater sensitivity [64]. Figure 8 provides significant insight into $\Delta\theta$ as a function of θ with different transmittances T to investigate the influence of photon loss. We can see from Fig. 8 that increasing photon loss leads to a higher bound of $\Delta\theta$, which means worse sensitivity. Compared to Fig. 3, the photon loss deteriorates $\Delta\theta$ and generates a “gap” for $\theta \rightarrow 0$. The broader gap makes estimating a small phase shift challenging. We show $\Delta\theta$ versus N with the influence of the photon loss in Fig. 9. Both Gaussian and non-Gaussian states experience sensitivity far from the $1/N$ and $1/\sqrt{N}$ limits. Another result of Fig. 9 is that the TMSV state is fragile to the influence of photon loss, and the PSA state shows its robustness. For $T = 0.5$, the TMSV state shows the worst $\Delta\theta$, although it is the best input state without noise, according to Figs. 2, 3, and 5.

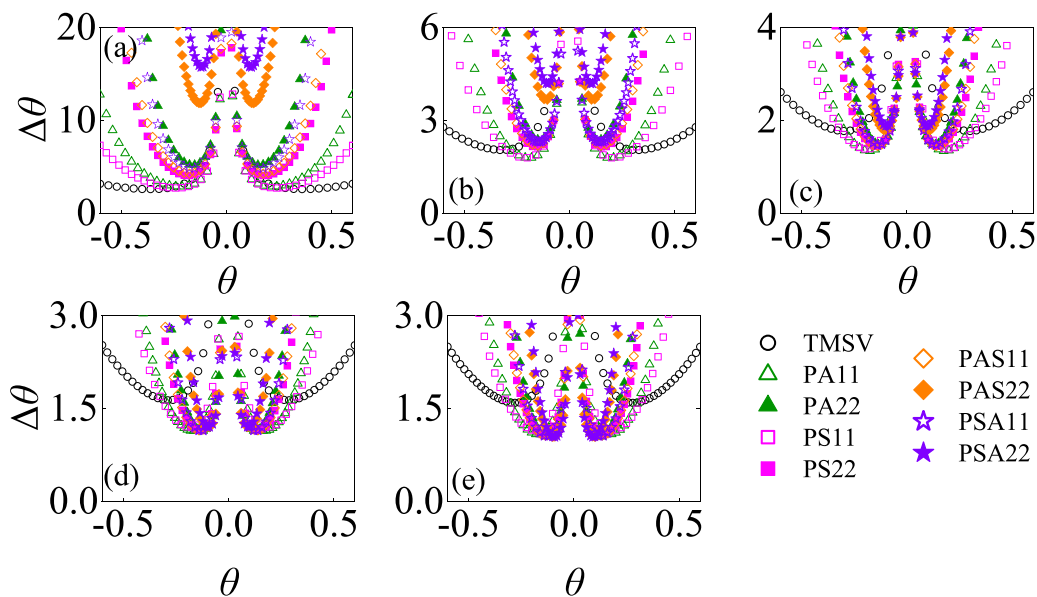


FIG. 7. Phase-estimation sensitivity as a function of phase shift with various photon losses. (a)–(e) represent $T_{a(b)} = 0.1(0.9)$, $T_{a(b)} = 0.2(0.8)$, $T_{a(b)} = 0.3(0.7)$, $T_{a(b)} = 0.4(0.6)$, and $T_{a(b)} = 0.5(0.5)$, respectively. The squeezing parameter is taken as $r = 1.096$.

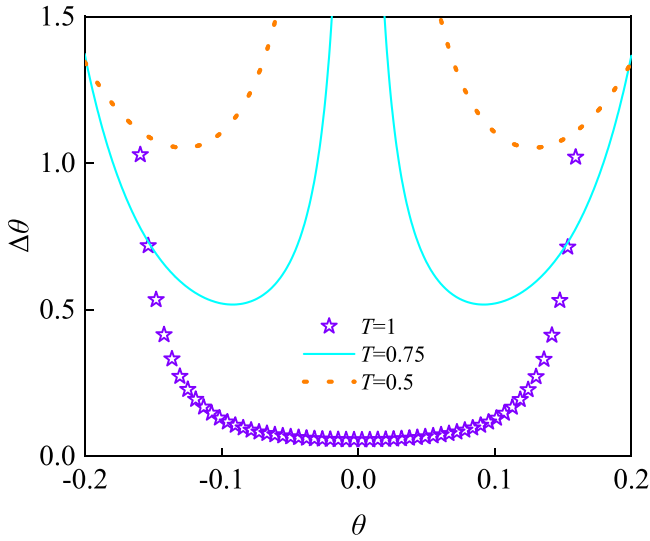


FIG. 8. The sensitivity as a function of θ for the PSA11 state; the squeezing parameter has been taken as $r = 1.096$. Stars denote $\Delta\theta$ without the photon loss. The solid line and dots represent $\Delta\theta$ for $T = 0.75$ and 0.5 , respectively.

B. OAM mitigation of the influence of the photon loss

From the discussion above, our results demonstrate that the increase in noise causes deterioration of the phase estimation for small phase shifts. To mitigate the deterioration caused by photon loss, we employ a non-Gaussian state enhanced by OAM.

A possible explanation for the gap that occurs in the presence of photon loss might be that the noise could be magnified at the near-decorrelation point ($\theta \rightarrow 0$) [65–67]. As shown in Fig. 10, with the increase of topological charge L , the sensitivity $\Delta\theta$ reaches lower bounds for transmittance $T = 0.5$. At the same time, the gap of the curve for $\theta \rightarrow 0$ gets narrower

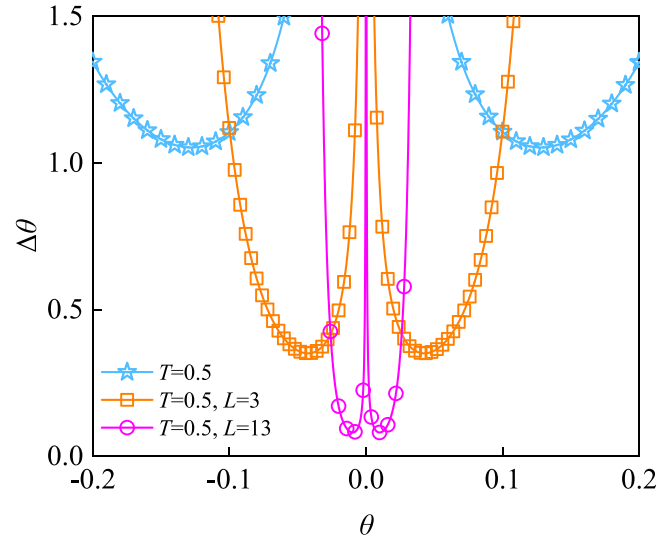


FIG. 10. The phase-estimation sensitivity $\Delta\theta$ as a function of the phase θ of the PSA11 state. The squeezing parameter has been taken as $r = 1.096$. The solid line with stars represents the measurement with $T = 0.5$ without enhancement from OAM. The solid lines with squares and circles denote $\Delta\theta$ with transmittance parameter $T = 0.5$ for OAM quantum numbers $L = 3$ and 13 , respectively.

with the enhancement of L , which makes it easy to measure small phase shifts even with 50% photon loss in both arms of the MZI. Figure 10 reveals that we can further mitigate the deterioration with OAM.

Significant enhancement of OAM contributed by SPPs [68] makes it impossible to estimate small phase shifts with noise. Figure 11 demonstrates the sensitivity $\Delta\theta$ versus mean photon number N with 50% photon loss for $L = 21$. With the enhancement of OAM, $\Delta\theta$ surpasses the HL when $N < 15$

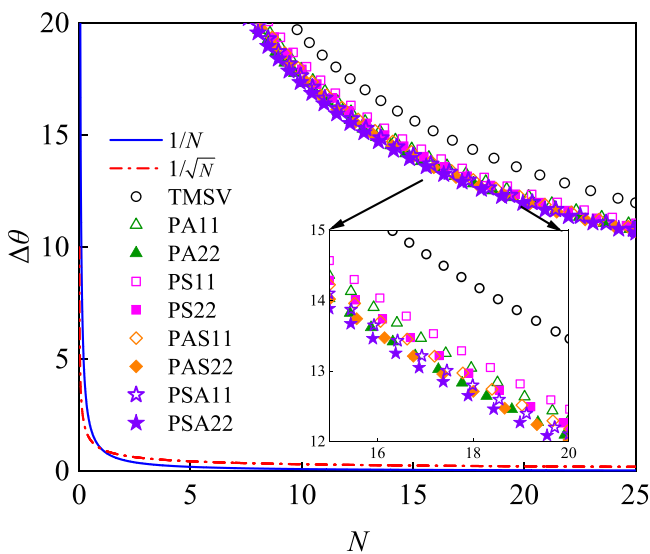


FIG. 9. The phase-estimation sensitivity $\Delta\theta$ versus mean photon number N for all input states. The transmittance parameter has been set to $T = 0.5$ for all cases. The phase-shift value has been taken as $\theta = 10^{-4}$.

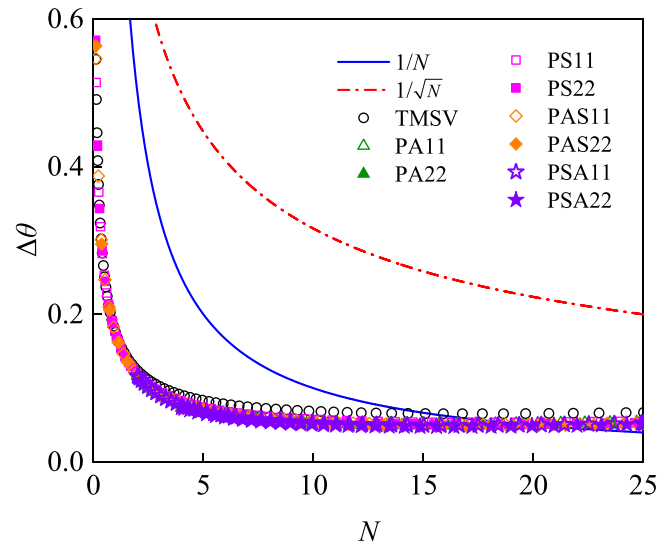


FIG. 11. Phase-estimation sensitivity of entanglement states $\Delta\theta$ as a function of the mean photon number N for all input states. The phase shift θ and OAM quantum number L have been taken as $\theta = 0.007$ and $L = 21$, respectively. The solid blue and red dash-dotted lines represent HL and SNL, respectively.

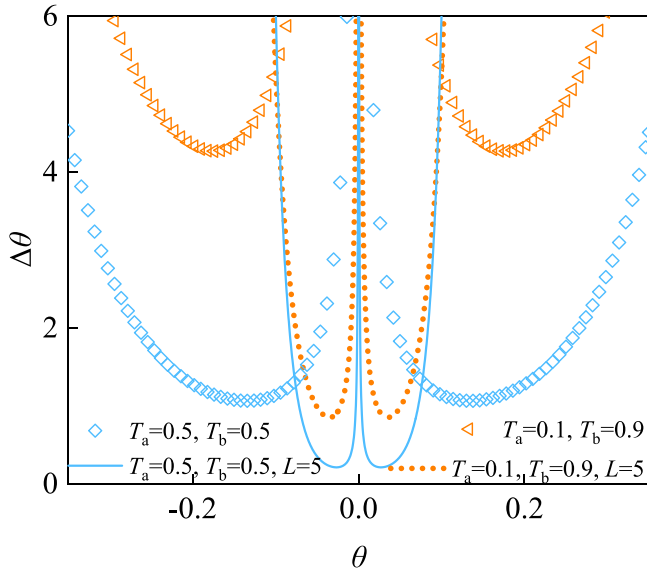


FIG. 12. Phase-estimation sensitivity $\Delta\theta$ as a function of the phase shift θ of the PAS11 state; the squeezing parameter has been taken as $r = 1.096$. The diamonds and solid line denote the measurement without the enhancement of OAM and $L = 5$, respectively, and the transmittance parameter is set to $T = 0.5$. Triangles and dots represent the phase shifts with no enhancement from OAM and the OAM quantum number $L = 5$, where the asymmetric photon loss $T_{a(b)} = 0.1$ (0.9).

for all input-state candidates. Remarkably, the enhancement of OAM can mitigate the deterioration caused by photon loss.

Figure 12 contrasts the impacts of OAM enhancement on symmetric and asymmetric photon losses. The findings reveal that, for a constant topological charge L , the phase-estimation sensitivity performs more optimally with symmetric noise than with asymmetric noise.

To display the effectiveness of OAM enhancement, we plot the sensitivity $\Delta\theta$ as a function of the mean photon number N with various photon losses. The result from Fig. 13 is clearly that for $\theta = 0.007$, the symmetric photon loss has the best sensitivity, which is a conclusion similar to that from Fig. 7. With topological charge $L = 21$, the phase-estimation sensitivity can readily surpass the $1/N$ limit without a significantly higher mean photon number.

IV. STATISTICAL PROPERTIES OF GAUSSIAN AND NON-GAUSSIAN STATES

In the protocol, the TMSV states can be described as [22,24]

$$\begin{aligned} |\Psi\rangle_{\text{TMSV}} &= \hat{S}(\xi)|n_1, n_2\rangle \\ &= \exp(\xi^* \hat{a} \hat{b} - \xi \hat{a}^\dagger \hat{b}^\dagger)|n_1, n_2\rangle \end{aligned} \quad (5)$$

where $\hat{S}(\xi)$ is the two-mode squeezing parameter and $\xi = r e^{i\psi}$, where r is the squeezing parameter and ψ is the squeezing angle. We illustrate the mean photon number of the proposed states as a function of the squeezing parameter in Fig. 14. As shown in Fig. 14, when $r \rightarrow 0$, the initial N of the non-Gaussian state is determined by the Bose operator acting on the TMSV state. The plot further elucidates that for a given

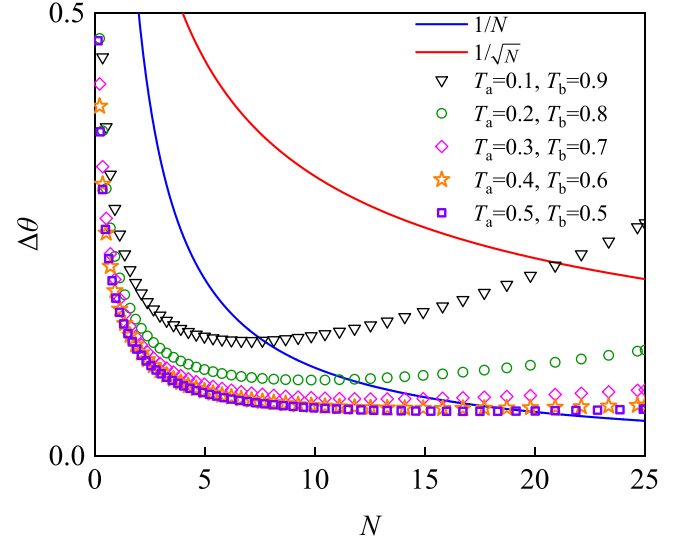


FIG. 13. Phase-estimation sensitivity $\Delta\theta$ versus mean photon number N with various photon losses for the PAS11 state. The phase-shift value and OAM quantum number are set as $\theta = 0.007$ and $L = 21$.

r , the TMSV state has the lowest N , while PSA22 has the highest N .

The properties of input states determine the result of measurement. We use von Neumann entropy as a witness of non-classical properties and entanglement [69,70]. Equations (6) gives the equation for entropy, where $\rho_a = \text{Tr}_b[|\Psi_{ab}\rangle\langle\Psi_{ab}|]$ and $\rho_b = \text{Tr}_a[|\Psi_{ab}\rangle\langle\Psi_{ab}|]$. We use the label E to represent entropy hereafter,

$$E(|\Psi_{ab}\rangle) = -\text{Tr}[\rho_a \ln(\rho_a)] = -\text{Tr}[\rho_b \ln(\rho_b)]. \quad (6)$$

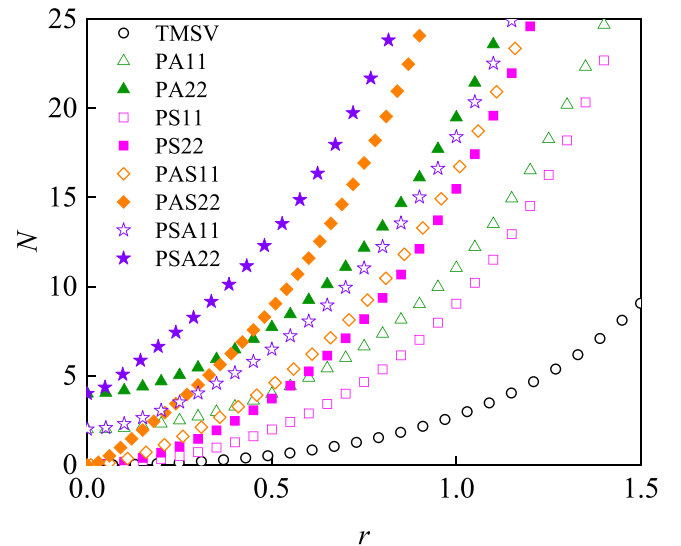


FIG. 14. Mean photon number as a function of the squeezing parameter for Gaussian and non-Gaussian states. Black circles denote the TMSV state; squares, triangles, diamonds, and stars indicate PS, PA, PAS and PSA, respectively. The open symbols represent low order $G = H = 1$, and solid symbols are for $G = H = 2$.

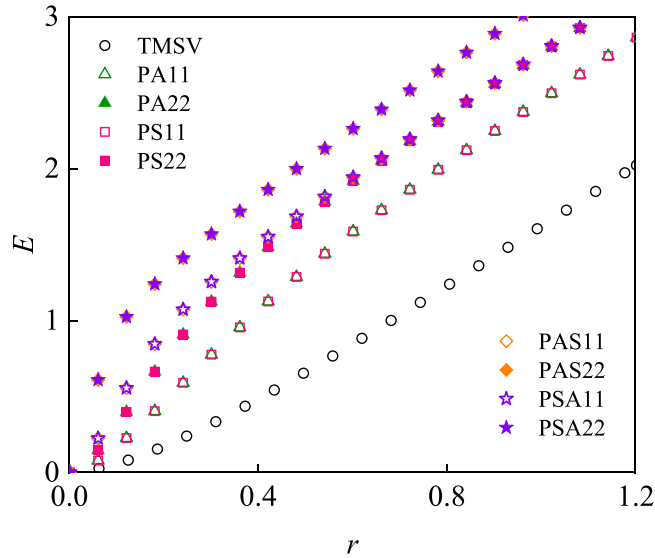


FIG. 15. von Neumann entropy as a function of the mean photon number. The black circles denote the TMSV state. PA, PS, PAS, and PSA are represented by triangles, squares, diamonds, and stars, respectively. The open symbols represent low order $G = H = 1$, and the solid symbols are for $G = H = 2$.

We use Eq. (6) to obtain the entropy as a function of r and show the result in Fig. 15. We can see from this plot that TMSV has the lowest entropy [71], while PAS22 and PSA22 have the largest.

In this study, we employ the parity measurement to enable high-sensitivity measurement. A parity measurement in one output mode is relevant to the detection of $\sum_{N=0}^{\infty} \sum_{M=0}^N |N - M, M\rangle\langle M, N - M|$ [18,26]. Consequently, the properties of the input state can be analyzed via joint photon number distribution. In Fig. 16, our primary focus lies on the PAS and PSA states due to their superior robustness in the presence of photon loss. Unlike the TMSV state, which exhibits a “thermal-like down the diagonal” distribution [72–74], the PAS and PSA states present a markedly different perspective. The maximum value of probability is located at $|8, 8\rangle$ (PAS) and $|9, 9\rangle$ (PSA). This distribution thus serves as a useful tool for distinguishing the non-Gaussian states we are working with.

To visualize the properties and distinguish different states and evolutions of the input states, we use the Wigner function [11,75–80]. We compare the initial input states in Figs. 17(a)–17(e). As we can see, non-Gaussian states have a negative value for the Wigner function in the center of the axis, which shows their nonclassical properties. Among all input states, the PSA state has the largest area of negativity, which indicates it has more nonclassical properties than the other states. This plot offers a useful way to identify which state has the best sensitivity in the presence of photon loss. In Figs. 17(f)–17(h), we compare the Wigner function of the PSA state with different OAM numbers after the first BS. As we can see, Fig. 17(f) shows the state with no enhancement from OAM, and Figs. 17(g) and 17(h) present the state with OAM of $L = 7$ and $L = 51$. With higher OAM, the plot of the state rotates with a larger angle.

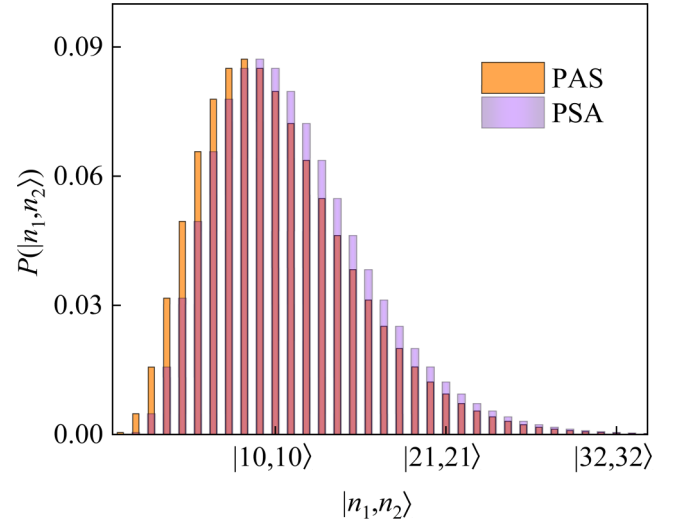


FIG. 16. The joint photon number distributions for the PAS (orange) and PSA (purple) states; the squeezing parameter is taken as $r = 1.096$.

V. CONCLUSION

In summary, we utilized OAM and non-Gaussian states to achieve higher sensitivity in phase estimation under significant noise. The non-Gaussian state, particularly the PSA state, exhibits higher sensitivity than the TMSV state. In order to further improve the sensitivity, we can balance the photon loss in the two arms of the MZI. With the presence of symmetric noise, non-Gaussian states with higher-order Bose operators achieve a lower sensitivity bound for small phase shift in the symmetric photon loss.

As noise levels escalate, the task of estimating small phase shifts becomes progressively more challenging. Nevertheless, an increase in topological charge results in the photon carrying a higher degree of OAM. This enhancement improves the resilience of the estimation scheme by mitigating the detrimental effects of noise, thereby facilitating the estimation of small phase shifts ($\theta \rightarrow 0$). This makes it feasible to achieve the $1/N$ limit, even in the face of substantial photon loss, such as 50% photon loss. Our research offers practical methodologies for realizing superior sensitivity in phase estimation under significant noise conditions. We anticipate that our findings will serve as a valuable and effective instrument in the field of quantum metrology.

ACKNOWLEDGMENTS

This work was supported by the National Natural Science Foundation of China (Grant No. 11675046), the Program for Innovation Research of Science in Harbin Institute of Technology (Grant No. A201412), and the Postdoctoral Scientific Research Developmental Fund of Heilongjiang Province (Grant No. LBH-Q15060). Our work is also supported by the Fundamental Research Funds for the Central Universities (Project No. 2023FRFK06012).

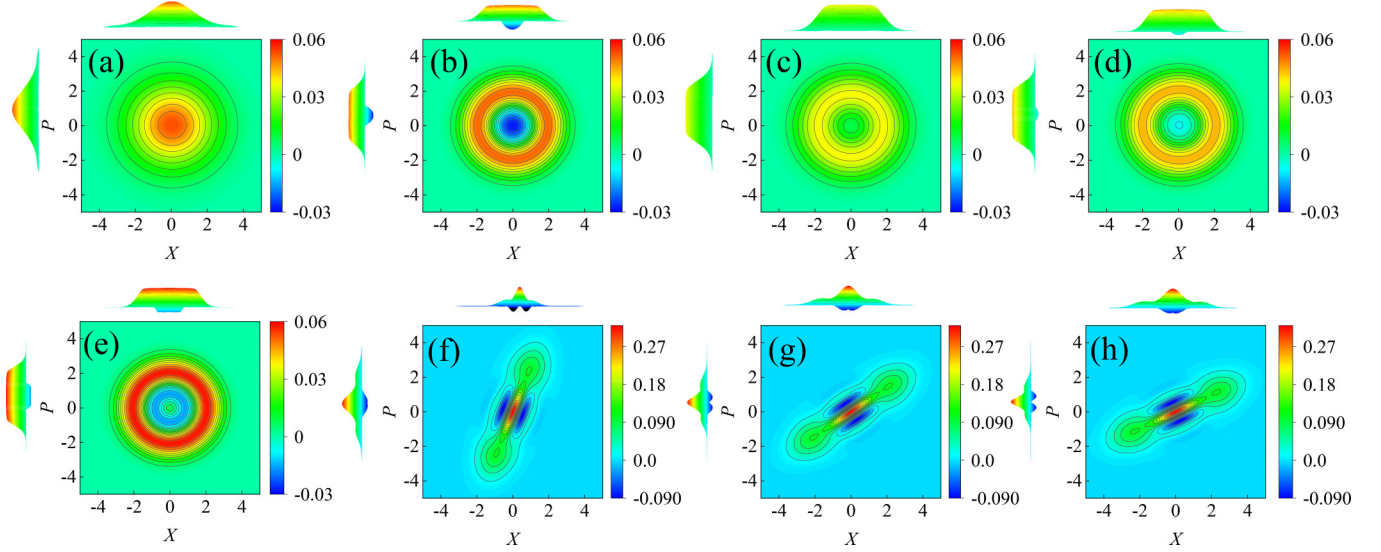


FIG. 17. Wigner-function plot of input states with mean photon number $N = 5$ and their evolution with different OAMs. (a)–(e) The Wigner-function plots of the TMSV, PA, PS, PAS, and PSA states, respectively. Data in (f)–(h) indicate the PSA state after the phase shift with no OAM enhancement, $L = 7$, and $L = 51$, respectively. In the top and left views of the plan diagram, we have provided the orthogonal and side views of the Wigner function, respectively.

APPENDIX A: SENSITIVITY BY PARITY DETECTION AND THE QCRB

As high-sensitivity quantum metrology, the well-known quantum Cramér-Rao bound (QCRB) determined by quantum Fisher information (QFI) has been studied by phase estimation. The QCRB can be obtained according to the input resource, and it is independent of detection, $\Delta\theta_{\text{QCRB}} = 1/\sqrt{F_Q}$, where F_Q denotes QFI. According to this theory, greater F_Q can achieve higher $\Delta\theta$. For an input state, F_Q can be calculated as

$$F_Q = 4[\langle \hat{\Psi}' | \hat{\Psi}' \rangle - \langle \hat{\Psi}' | \hat{\Psi} \rangle^2], \quad (\text{A1})$$

where $|\Psi\rangle = U_\theta U_{\text{BS1}} |\Psi_{\text{in}}\rangle$ represent the state vector after BS_1 and the DP and prior to the second beam splitter, BS_2 , and $|\hat{\Psi}'\rangle = \partial|\Psi\rangle/\partial\theta$. Equation (A1) becomes

$$F_Q = 4[\langle \Psi_{\text{in}} | \hat{J}_2^2 | \Psi_{\text{in}} \rangle - |\langle \Psi_{\text{in}} | \hat{J}_2 | \Psi_{\text{in}} \rangle|^2], \quad (\text{A2})$$

where $J_{1,2,3}$ represent the angular momentum operators:

$$\begin{aligned} \hat{J}_1 &= \frac{1}{2}(\hat{a}^\dagger \hat{b} + \hat{a} \hat{b}^\dagger), \quad \hat{J}_2 = \frac{1}{2i}(\hat{a}^\dagger \hat{b} - \hat{a} \hat{b}^\dagger), \\ \hat{J}_3 &= \frac{1}{2}(\hat{a}^\dagger \hat{a} - \hat{b}^\dagger \hat{b}). \end{aligned} \quad (\text{A3})$$

To thoroughly investigate the potential of the input resource, we plot the QCRB and sensitivity versus the mean photon number N in Fig. 18. We use diamonds and stars to represent the sensitivity of different input states and a dash-dotted line to represent the QCRB of the corresponding state. The open symbols denote the state with $G = H = 1$, and solid symbols represent states with $G = H = 2$. These results suggest that parity offers a good detection that can saturate the QCRB.

APPENDIX B: DERIVATION OF THE PARITY-DETECTION SIGNAL AND ITS SENSITIVITY

The non-Gaussian state is obtained by harnessing the Bose operator on the TMSV state represented by

$$\begin{aligned} |\hat{\Psi}\rangle_{\text{PAS}} &= \hat{a}^{\dagger G} \hat{b}^H \hat{S}|0, 0\rangle, \\ |\hat{\Psi}\rangle_{\text{PSA}} &= \hat{a}^G \hat{b}^{\dagger H} \hat{S}|0, 0\rangle. \end{aligned} \quad (\text{B1})$$

In the protocol, we use the parity-detection method. The parity operator can be represented in the coherence state, as shown in Eq. (B2), where $|\gamma\rangle$ is the coherent state:

$$\hat{\Pi}_b = (-1)^{\hat{n}} = e^{i\pi \hat{b}^\dagger \hat{b}} = \int \frac{d^2x}{\pi} |\gamma\rangle \langle -\gamma|. \quad (\text{B2})$$

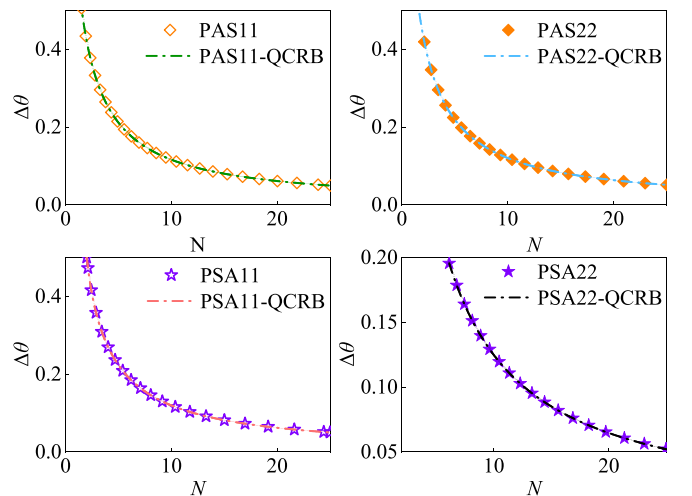


FIG. 18. Phase-estimation sensitivity of the PAS and PSA states and their QCRB in the absence of noise. Diamonds and stars represent the PAS state and the PSA state. The hollow icons represent low order $G = H = 1$ and solid icons for $G = H = 2$.

After harnessing the parity operator on the output state, the expectation value of the detection signal can be represented as

$$\langle \Pi_b \rangle = {}_{\text{out}} \langle \Psi | \int \frac{d^2x}{\pi} |\gamma\rangle \langle -\gamma | | \Psi \rangle_{\text{out}}. \quad (\text{B3})$$

We can also represent Gaussian and non-Gaussian states in the coherence state; here, we take the TMSV as an example, where $z = \tanh(r)$:

$$|\Psi\rangle_{\text{TMSV}} = (1 - z^2)^{\frac{1}{2}} \int \frac{d^2\alpha d^2\beta}{\pi^2} \exp\left[-\frac{|\alpha|^2 |\beta|^2}{2} + \alpha^* \beta^* z\right] \times |\alpha, \beta\rangle. \quad (\text{B4})$$

The evolution can be represented by a unitary operator, and the evolution of the input state can be simplified as the evolution of the Bose operator. After representing input states in the basis of the coherent state, the state's evolution can be calculated as follows:

$$e^{\xi \hat{A}} \hat{B} e^{-\xi \hat{A}} = \hat{B} + \xi [\hat{A}, \hat{B}] + \frac{\xi^2}{2!} [\hat{A}, [\hat{A}, \hat{B}]] + \dots \quad (\text{B5})$$

In the absence of photon loss, the evolution can be represented as

$$\begin{aligned} U_{\text{MZI}}^\dagger \hat{a}^\dagger U_{\text{MZI}} &= \hat{a}^\dagger \cos \frac{\theta}{2} + \hat{b}^\dagger \sin \frac{\theta}{2}, \\ U_{\text{MZI}}^\dagger \hat{b}^\dagger U_{\text{MZI}} &= \hat{b}^\dagger \cos \frac{\theta}{2} - \hat{a}^\dagger \sin \frac{\theta}{2}. \end{aligned} \quad (\text{B6})$$

In order to calculate photon loss, we introduce two fictitious beam splitters (BSL1 and BSL2) into the path of the MZI system. After the evolution, including photon loss, we obtain the reduced density matrix by tracing over the environmental modes that have passed through the beam splitter. In the presence of the photon loss, the evolution of the lossy MZI protocol can be represented as [38]

$$\begin{aligned} U_{\text{MZI}}^\dagger \hat{a}^\dagger U_{\text{MZI}} &= \frac{1}{2} \left[\hat{a}^\dagger \cos \frac{\theta}{2} (\cos Q_a + \cos Q_b) \right. \\ &\quad + i \hat{b}^\dagger \cos \frac{\theta}{2} (\cos Q_a - \cos Q_b) \\ &\quad + i \hat{a}^\dagger \sin \frac{\theta}{2} (\cos Q_b - \cos Q_a) \\ &\quad \left. + \hat{b}^\dagger \sin \frac{\theta}{2} (\cos Q_b + \cos Q_a) \right], \\ U_{\text{MZI}}^\dagger \hat{b}^\dagger U_{\text{MZI}} &= \frac{1}{2} \left[i \hat{a}^\dagger \cos \frac{\theta}{2} (\cos Q_b - \cos Q_a) \right. \\ &\quad + \hat{b}^\dagger \cos \frac{\theta}{2} (\cos Q_a + \cos Q_b) \\ &\quad + \hat{a}^\dagger \sin \frac{\theta}{2} (-\cos Q_a - \cos Q_b) \\ &\quad \left. + i \hat{b}^\dagger \sin \frac{\theta}{2} (\cos Q_b - \cos Q_a) \right], \end{aligned} \quad (\text{B7})$$

where $\cos^2 Q_a = T_a$ and $\cos^2 Q_b = T_b$. By using Eq. (B7) and the integral below, we can derive the parity-detection signal:

$$\begin{aligned} &\int \frac{d^2z}{\pi} \exp[\zeta |z|^2 + \xi z + \eta z^* + fz^2 + gz^{*2}] \\ &= \frac{1}{\sqrt{\zeta^2 - 4fg}} \exp\left[\frac{-\zeta\xi\eta + \xi^2g + \eta^2f}{\zeta^2 - 4fg}\right]. \end{aligned} \quad (\text{B8})$$

According to Eqs. (B3), (B7), and (B8), we obtain the parity signal of the output state enhanced by OAM in a lossy MZI system. In the presence of noise, the equation is too long to demonstrate. We assume $T = 1$ (no noise) and give the equation of PSA11 sensitivity as

$$\begin{aligned} \Delta\theta_{\text{PSA11}(\theta+\pi/2)} &= (1 - [z^4(-1 + z^2)^2\{-4 * (2 \\ &\quad - 63z^4 + 39z^8 + 14z^{12})\cos L(\pi \\ &\quad + 2\theta) + z^2[-4 + 315z^4 - 252z^8 \\ &\quad + 8z^{12} + 4 * (15 - 41z^4 + 9z^8) \\ &\quad \times \cos 2L(\pi + 2\theta) + 4z^2(-9 + z^4) \\ &\quad \times \cos 3L(\pi + 2\theta) + z^4 \cos 4L(\pi \\ &\quad + 2\theta)\}^2]/\{64(1 + z^4 + 2z^2 \\ &\quad \times \cos 2L\theta)[1 + z^4 + 2z^2 \cos L(\pi \\ &\quad + 2\theta)]\}^{\frac{1}{2}} / (2\{|Lz^2(-1 + z^2) \\ &\quad \times [1 - 51z^4 + 396z^8 - 245z^{12} \\ &\quad + 15z^{16} - 6z^2(6 - 49z^4 + 10z^8 \\ &\quad + 10z^{12})\cos L(\pi + 2\theta) + 3z^4(19 \\ &\quad - 20z^4 + 5z^8)\cos 2L(\pi + 2\theta) \\ &\quad - 10z^6 \cos 3L(\pi + 2\theta)]\sin L(\pi \\ &\quad + 2\theta)\} / \{(1 + z^4 + 2z^2 \\ &\quad \times \cos 2L\theta)^{\frac{1}{2}} [1 + z^4 + 2z^2 \cos L(\pi + 2\theta)]\}^5)]. \end{aligned} \quad (\text{B9})$$

The parity signal of the PAS11 state is

$$\begin{aligned} \langle \Pi \rangle_{\text{PAS}(\theta+\pi/2)} &= \{(1 - z^2)[8 - 252z^4 + 315z^8 \\ &\quad - 4z^{12} - 4z^2(14 + 39z^4 63z^8 \\ &\quad + 2z^{12})\cos L(\pi + 2\theta) + 4z^4(9 \\ &\quad - 41z^4 + 15z^8)\cos 2L(\pi + 2\theta) \\ &\quad + 4z^6 \cos 3L(\pi + 2\theta) - 36z^{10} \\ &\quad \times \cos 3L(\pi + 2\theta) + z^8 \cos 4L(\pi \\ &\quad + 2\theta)]\} / \{8(1 + z^4 + 2z^2 \\ &\quad \times \cos 2L\theta)^{\frac{1}{2}} [1 + z^4 + 2z^2 \cos L(\pi + 2\theta)]\}. \end{aligned} \quad (\text{B10})$$

The sensitivity of the PAS11 state is represented as

$$\begin{aligned} \Delta\theta_{\text{PAS11}(\theta+\pi/2)} &= (1 - \{(-1 + z^2)^2[8 - 252z^4 \\ &\quad + 315z^8 - 4z^{12} - 4z^2(14 + 39z^4 \end{aligned}$$

$$\begin{aligned}
& -63z^8 + 2z^{12}) \cos L(\pi + 2\theta) \\
& + 4z^4(9 - 41z^4 + 15z^8) \cos 2L(\pi \\
& + 2\theta) + 4z^6 \cos 3L(\pi + 2\theta) \\
& - 36z^{10} \cos 3L(\pi + 2\theta) + z^8 \\
& \times \cos 4L(\pi + 2\theta)] / \{64(1 + z^4 \\
& + 2z^2 \cos 2L\theta)[1 + z^4 + 2z^2 \\
& \times \cos L(\pi + 2\theta)]\}^{\frac{1}{2}} / (2|Lz^2 \\
& \times (-1 + z^2)[15 - 245z^4 + 396z^8 \\
& - 51z^{12} + z^{16} - 6z^2(10 + 10z^4 \\
& - 49z^8 + 6z^{12}) \cos L(\pi + 2\theta) \\
& + 3z^4(5 - 20z^4 + 19z^8) \\
& \times \cos 2L(\pi + 2\theta) - 10z^{10} \cos 3L(\pi \\
& + 2\theta)] \sin L(\pi + 2\theta)] / \{(1 + z^4 \\
& + 2z^2 \cos 2L\theta)^{\frac{1}{2}} [1 + z^4 \\
& + 2z^2 \cos L(\pi 2\theta)]^5\}. \quad (\text{B11})
\end{aligned}$$

In the presence of photon loss, e.g., $T_a, T_b \neq 1$, the equations for the PAS and PSA states are too long to present. We here present the sensitivity of the PS11 state as an example:

$$\begin{aligned}
\langle \Pi \rangle_{\text{PS11}(\theta+\pi/2)} &= [8z^2(-1 + z^2) \{ -128 + 32z^2 - 32T_a^2 z^2 \\
& + 16T_a^2 z^2 - 32T_b^2 + 16T_b^2 z^2 - 12z^4 \\
& + 16T_a z^4 + 8T_a^3 z^4 - 2T_a^4 z^4 - 16\sqrt{T_a T_b} z^4 \\
& + 64T_a^{3/2} \sqrt{T_b} z^4 + 16T_b z^4 + 56T_a T_b z^4 \\
& + 8T_a^2 T_b z^4 + 64\sqrt{T_a} T_b^{3/2} z^4 - 16T_a^{3/2} T_b^{3/2} z^4 \\
& + 8T_a T_b^2 z^4 - 8T_a^2 T_b^2 z^4 + 8T_b^3 z^4 \\
& - 2T_b^4 z^4 - 2T_a^2 z^6 + 2T_a^3 z^6 - T_a^4 z^6 \\
& - 8T_a^{3/2} \sqrt{T_b} z^6 + 8T_a^{5/2} \sqrt{T_b} z^6 \\
& - 4T_a^{7/2} \sqrt{T_b} z^6 - 12T_a T_b z^6 \\
& + 14T_a^2 T_b z^6 - 6T_a^3 T_b z^6 - 8\sqrt{T_a} \\
& \times T_b^{3/2} z^6 + 16T_a^{3/2} T_b^{3/2} z^6 - 4T_a^{5/2} \\
& \times T_b^{3/2} z^6 z^6 - 2T_b^2 z^6 + 14T_a T_b^2 z^6 \\
& - 2T_a^2 T_b^2 z^6 + 8\sqrt{T_a} T_b^{5/2} z^6 - 4T_a^{3/2} \\
& \times T_b^{5/2} z^6 + 2T_b^3 z^6 - 6T_a T_b^3 z^6 \\
& - 4\sqrt{T_a} T_b^{7/2} z^6 - T_b^4 z^6 + 2(z \\
& + \sqrt{T_a} T_b z)^2 [-16 + 4 * (2 - 2T_a \\
& + T_a^2 - 2T_b + T_b^2) z^2 + (\sqrt{T_a} \\
& + \sqrt{T_b})^4 z^4] \cos L(\pi + 2\theta) - 4(z \\
& + \sqrt{T_a T_b} z)^4 \cos 2L(\pi \\
& + 2\theta) \} / \{ [16 - 4(2 - 2T_a \\
& + T_a^2 - 2T_b + T_b^2) z^2 + (\sqrt{T_a} \\
& + \sqrt{T_b})^4 z^4 + 8(z + \sqrt{T_a T_b} z)^2 \\
& \times \cos 2L\theta]^{1/2} [16 - 4(2 - 2T_a + T_a^2 \\
& - 2T_b + T_b^2) z^2 + (\sqrt{T_a} + \sqrt{T_b})^4 z^4 \\
& + 8(z + \sqrt{T_a T_b} z)^2 \cos L(\pi + 2\theta)]^2 \}. \quad (\text{B12})
\end{aligned}$$

-
- [1] M. Tse *et al.*, Quantum-Enhanced Advanced LIGO Detectors in the Era of Gravitational-Wave Astronomy, *Phys. Rev. Lett.* **123**, 231107 (2019).
- [2] K. M. Backes *et al.*, A quantum enhanced search for dark matter axions, *Nature (London)* **590**, 238 (2021).
- [3] S. Hong, J. Rehman, Y.-S. Kim, Y.-W. Cho, S.-W. Lee, H. Jung, S. Moon, S.-W. Han, and H.-T. Lim, Quantum enhanced multiple-phase estimation with multi-mode N00N states, *Nat. Commun.* **12**, 5211 (2021).
- [4] W. Górecki and R. Demkowicz-Dobrzański, Multiple-Phase Quantum Interferometry: Real and Apparent Gains of Measuring All the Phases Simultaneously, *Phys. Rev. Lett.* **128**, 040504 (2022).
- [5] R. Okamoto and T. Tahara, Precision limit for simultaneous phase and transmittance estimation with phase-shifting interferometry, *Phys. Rev. A* **104**, 033521 (2021).
- [6] G.-F. Jiao, Q. Wang, Z. F. Yu, L. Q. Chen, W. P. Zhang, and C.-H. Yuan, Effects of losses on the sensitivity of an actively correlated Mach-Zehnder interferometer, *Phys. Rev. A* **104**, 013725 (2021).
- [7] S. K. Chang, W. Ye, H. Zhang, L. Y. Hu, J. H. Huang, and S. Q. Liu, Improvement of phase sensitivity in an SU(1,1) interferometer via a phase shift induced by a Kerr medium, *Phys. Rev. A* **105**, 033704 (2022).
- [8] J. M. Kwolek and A. T. Black, Continuous Sub-Doppler-Cooled Atomic Beam Interferometer for Inertial Sensing, *Phys. Rev. Appl.* **17**, 024061 (2022).
- [9] J.-D. Zhang, C. You, C. Li, and S. Wang, Phase sensitivity approaching the quantum Cramér-Rao bound in a modified SU(1,1) interferometer, *Phys. Rev. A* **103**, 032617 (2021).
- [10] W. Ge, K. Jacobs, Z. Eldredge, A. V. Gorshkov, and M. Foss-Feig, Distributed Quantum Metrology with Linear Networks and Separable Inputs, *Phys. Rev. Lett.* **121**, 043604 (2018).
- [11] H. Zhang, W. Ye, C. Wei, Y. Xia, S. Chang, Z. Liao, and L. Y. Hu, Improved phase sensitivity in a quantum optical interferometer based on multiphoton catalytic two-mode squeezed vacuum states, *Phys. Rev. A* **103**, 013705 (2021).
- [12] S. Pang and A. N. Jordan, Optimal adaptive control for quantum metrology with time-dependent Hamiltonians, *Nat. Commun.* **8**, 14695 (2017).
- [13] S. Wang and J.-D. Zhang, Hermitian operator of a Mach-Zehnder interferometer combined with parity detection and its applications, *Opt. Commun.* **527**, 128987 (2023).

- [14] Y.-F. Guo, W. Zhong, L. Zhou, and Y.-B. Sheng, Supersensitivity of Kerr phase estimation with two-mode squeezed vacuum states, *Phys. Rev. A* **105**, 032609 (2022).
- [15] W. Zhong, L. Zhou, and Y.-B. Sheng, Double-port measurements for robust quantum optical metrology, *Phys. Rev. A* **103**, 042611 (2021).
- [16] C. Kumar, Rishabh, and S. Arora, Realistic non-Gaussian-operation scheme in parity-detection-based Mach-Zehnder quantum interferometry, *Phys. Rev. A* **105**, 052437 (2022).
- [17] H. Kwon, Kok C. Tan, T. Volkoff, and H. Jeong, Nonclassicality as a Quantifiable Resource for Quantum Metrology, *Phys. Rev. Lett.* **122**, 040503 (2019).
- [18] P. M. Anisimov, G. M. Raterman, A. Chiruvelli, W. N. Plick, S. D. Huver, H. Lee, and J. P. Dowling, Quantum Metrology with Two-Mode Squeezed Vacuum: Parity Detection Beats the Heisenberg Limit, *Phys. Rev. Lett.* **104**, 103602 (2010).
- [19] M. Walschaers, V. Parigi, and N. Treps, Practical framework for conditional non-Gaussian quantum state preparation, *PRX Quantum* **1**, 020305 (2020).
- [20] D. Zhang, Y. Cai, Z. Zheng, D. Barral, Y. Zhang, M. Xiao, and K. Bencheikh, Non-Gaussian nature and entanglement of spontaneous parametric nondegenerate triple-photon generation, *Phys. Rev. A* **103**, 013704 (2021).
- [21] K. Xu, Y. R. Zhang, Z. H. Sun, H. Li, P. T. Song, Z. C. Xiang, K. X. Huang, H. Li, Y. H. Shi, C. T. Chen, X. H. Song, D. N. Zheng, F. Nori, H. Wang, and H. Fan, Metrological Characterization of Non-Gaussian Entangled States of Superconducting Qubits, *Phys. Rev. Lett.* **128**, 150501 (2022).
- [22] M. Walschaers, Non-gaussian quantum states and where to find them, *PRX Quantum* **2**, 030204 (2021).
- [23] M. S. Tian, Y. Xiang, F. X. Sun, M. Fadel, and Q. Y. He, Characterizing Multipartite Non-Gaussian Entanglement for a Three-Mode Spontaneous Parametric Down-Conversion Process, *Phys. Rev. Appl.* **18**, 024065 (2022).
- [24] L. F. Fan and M. S. Zubairy, Quantum illumination using non-Gaussian states generated by photon subtraction and photon addition, *Phys. Rev. A* **98**, 012319 (2018).
- [25] S. Bose and M. S. Kumar, Analysis of necessary and sufficient conditions for quantum teleportation with non-Gaussian resources, *Phys. Rev. A* **103**, 032432 (2021).
- [26] L. Hu, M. Al-amri, Z. Liao, and M. S. Zubairy, Continuous-variable quantum key distribution with non-Gaussian operations, *Phys. Rev. A* **102**, 012608 (2020).
- [27] J. Singh and S. Bose, Non-Gaussian operations in measurement-device-independent quantum key distribution, *Phys. Rev. A* **104**, 052605 (2021).
- [28] Y. Baamara, A. Sinatra, and M. Gessner, Scaling Laws for the Sensitivity Enhancement of Non-Gaussian Spin States, *Phys. Rev. Lett.* **127**, 160501 (2021).
- [29] Y. Ouyang, S. Wang, and L.J. Zhang, Quantum optical interferometry via the photon-added two-mode squeezed vacuum states, *J. Opt. Soc. Am. B* **33**, 1373 (2016).
- [30] S. Wang, X. X. Xu, Y. J. Xu, and L. J. Zhang, Quantum interferometry via a coherent state mixed with a photon-added squeezed vacuum state, *Opt. Commun.* **444**, 102 (2019).
- [31] S. Ataman, A. Preda, and R. Ionicioiu, Phase sensitivity of a Mach-Zehnder interferometer with single-intensity and difference-intensity detection, *Phys. Rev. A* **98**, 043856 (2018).
- [32] W. J. Lu, L. Shao, X. Y. Zhang, Z. C. Zhang, J. Chen, H. Tao, and X. G. Wang, Extreme expected values and their applications in quantum metrology, *Phys. Rev. A* **105**, 023718 (2022).
- [33] A. Alodjants, D. Tsarev, T. V. Ngo, and R.K. Lee, Enhanced nonlinear quantum metrology with weakly coupled solitons in the presence of particle losses, *Phys. Rev. A* **105**, 012606 (2022).
- [34] G. S. Thekkadath, M. E. Mycroft, B. A. Bell, C. G. Wade, A. Eckstein, D. S. Phillips, R. B. Patel, A. Buraczewski, A. E. Lita, T. Gerrits, S. W. Nam, M. Stobińska, A. I. Lvovsky, and I. A. Walmsley, Quantum-enhanced interferometry with large heralded photon-number states, *npj Quantum Inf.* **6**, 89 (2020).
- [35] D. Gatto, P. Facchi, and V. Tamma, Heisenberg-limited estimation robust to photon losses in a Mach-Zehnder network with squeezed light, *Phys. Rev. A* **105**, 012607 (2022).
- [36] C. Oh, C. Lee, S. H. Lie, and H. Jeong, Optimal distributed quantum sensing using Gaussian states, *Phys. Rev. Res.* **2**, 023030 (2020).
- [37] G. Frascella, S. Agne, F. Y. Khalili, and M. V. Chekhova, Overcoming detection loss and noise in squeezing-based optical sensing, *npj Quantum Inf.* **7**, 72 (2021).
- [38] M. Barbieri, Optical quantum metrology, *PRX Quantum* **3**, 010202 (2022).
- [39] S. U. Shringarpure, C. M. Nunn, T. B. Pittman, and J. D. Franson, Coherence of quantum states after noiseless attenuation, *Phys. Rev. A* **105**, 013704 (2022).
- [40] M. Hiekkämäki, F. Bouchard, and R. Fickler, Photonic Angular Superresolution Using Twisted NOON States, *Phys. Rev. Lett.* **127**, 263601 (2021).
- [41] K. Liu, C. X. Cai, J. Li, L. Ma, H. X. Sun, and J. R. Gao, Squeezing-enhanced rotating-angle measurement beyond the quantum limit, *Appl. Phys. Lett.* **113**, 261103 (2018).
- [42] I. Nape, N. Mashaba, N. Mphuthi, S. Jayakumar, S. Bhattacharya, and A. Forbes, Vector-Mode Decay in Atmospheric Turbulence: An Analysis Inspired by Quantum Mechanics, *Phys. Rev. Appl.* **15**, 034030 (2021).
- [43] S. Ataman, Optimal Mach-Zehnder phase sensitivity with Gaussian states, *Phys. Rev. A* **100**, 063821 (2019).
- [44] T. Linowski, C. Gneiting, and Ł. Rudnicki, Stabilizing entanglement in two-mode Gaussian states, *Phys. Rev. A* **102**, 042405 (2020).
- [45] A. Hertz, N. J. Cerf, and S. De Bièvre, Relating the entanglement and optical nonclassicality of multimode states of a bosonic quantum field, *Phys. Rev. A* **102**, 032413 (2020).
- [46] S. Choudhury, R. M. Gharat, S. Mandal, N. Pandey, A. Roy, and P. Sarker, Entanglement in interacting quenched two-body coupled oscillator system, *Phys. Rev. D* **106**, 025002 (2022).
- [47] M. Poxleitner and H. Hinrichsen, Gaussian continuous-variable isotropic state, *Phys. Rev. A* **104**, 032423 (2021).
- [48] N. Namekata, Y. Takahashi, G. Fujii, D. Fukuda, S. Kurimura, and S. Inoue, Non-Gaussian operation based on photon subtraction using a photon-number-resolving detector at a telecommunications wavelength, *Nat. Photon.* **4**, 655 (2010).
- [49] L.Y. Hu, Z. Y. Liao, and M. S. Zubairy, Continuous-variable entanglement via multiphoton catalysis, *Phys. Rev. A* **95**, 012310 (2017).
- [50] L. Hu, M. Al-amri, Z. Liao, and M. S. Zubairy, Entanglement improvement via a quantum scissor in a realistic environment, *Phys. Rev. A* **100**, 052322 (2019).

- [51] Y. Guo, W. Ye, H. Zhong, and Q. Liao, Continuous-variable quantum key distribution with non-Gaussian quantum catalysis, *Phys. Rev. A* **99**, 032327 (2019).
- [52] Y. Zhao, Y. Zhang, B. Xu, S. Yu, and H. Guo, Continuous-variable measurement-device-independent quantum key distribution with virtual photon subtraction, *Phys. Rev. A* **97**, 042328 (2018).
- [53] H. X. Ma, P. Huang, D. Y. Bai, S. Y. Wang, W. S. Bao, and G. H. Zeng, Continuous-variable measurement-device-independent quantum key distribution with photon subtraction, *Phys. Rev. A* **97**, 042329 (2018).
- [54] V. Parigi, A. Zavatta, M. Kim, and M. Bellini, Probing quantum commutation rules by addition and subtraction of single photons to/from a light field, *Science* **317**, 1890 (2007).
- [55] S.-Y. Lee and H. Nha, Second-order superposition operations via Hong-Ou-Mandel interference, *Phys. Rev. A* **85**, 043816 (2012).
- [56] Y. H. Wen, I. Chremmos, Y. J. Chen, Y. F. Zhang, and S. Y. Yu, Arbitrary Multiplication and Division of the Orbital Angular Momentum of Light, *Phys. Rev. Lett.* **124**, 213901 (2020).
- [57] X. Jiang, D. Ta, and W. Q. Wang, Modulation of Orbital-Angular-Momentum Symmetry of Nondiffractive Acoustic Vortex Beams and Realization Using a Metasurface, *Phys. Rev. Appl.* **14**, 034014 (2020).
- [58] Z. Y. Mao, H. G. Liu, and X. F. Chen, Active Control of Interconversion of Spin and Orbital Angular Momentum of Light by a Scattering System, *Phys. Rev. Appl.* **18**, 024061 (2022).
- [59] Z. B. Huang, P. P. Wang, J. M. Liu, W. J. Xiong, Y. L. He, J. G. Xiao, H. P. Ye, Y. Li, S. Q. Chen, and D. Y. Fan, All-Optical Signal Processing of Vortex Beams with Diffractive Deep Neural Networks, *Phys. Rev. Appl.* **15**, 014037 (2021).
- [60] A. Chong, C. H. Wan, J. Chen, and Q. W. Zhan, Generation of spatiotemporal optical vortices with controllable transverse orbital angular momentum, *Nat. Photon.* **14**, 350 (2020).
- [61] Z. X. Huang, K. R. Motes, P. M. Anisimov, J. P. Dowling, and D. W. Berry, Adaptive phase estimation with two-mode squeezed vacuum and parity measurement, *Phys. Rev. A* **95**, 053837 (2017).
- [62] K. P. Seshadreesan, S. Kim, J. P. Dowling, and H. Lee, Phase estimation at the quantum Cramér-Rao bound via parity detection, *Phys. Rev. A* **87**, 043833 (2013).
- [63] K. P. Seshadreesan, P. M. Anisimov, H. Lee, and J. P. Dowling, Parity detection achieves the Heisenberg limit in interferometry with coherent mixed with squeezed vacuum light, *New J. Phys.* **13**, 083026 (2011).
- [64] S. Bose and H. Jeong, Quantum teleportation of hybrid qubits and single-photon qubits using gaussian resources, *Phys. Rev. A* **105**, 032434 (2022).
- [65] H. Zhang, W. Ye, C. P. Wei, C. J. Liu, Z. Y. Liao, and L. Y. Hu, Improving phase estimation using number-conserving operations, *Phys. Rev. A* **103**, 052602 (2021).
- [66] D. Li, C.-H. Yuan, Y. Yao, W. Jiang, M. Li, and W. Zhang, Effects of loss on the phase sensitivity with parity detection in an SU(1,1) interferometer, *J. Opt. Soc. Am. B* **35**, 1080 (2018).
- [67] Z. D. Chen, C. H. Yuan, H. M. Ma, D. Li, L. Q. Chen, Z. Y. Ou, and W. P. Zhang, Effects of losses in the atom-light hybrid SU(1,1) interferometer, *Opt. Express* **24**, 17766 (2016).
- [68] J. Wang, A. Cao, M. Zhang, H. Pang, S. Hu, Y. Fu, L. Shi, and Q. Deng, Study of characteristics of vortex beam produced by fabricated spiral phase plates, *IEEE Photonics J.* **8**, 1 (2016).
- [69] P. Boes, J. Eisert, R. Gallego, M. P. Müller, and H. Wilming, von Neumann Entropy from Unitarity, *Phys. Rev. Lett.* **122**, 210402 (2019).
- [70] L. Wei, Exact variance of von Neumann entanglement entropy over the Bures-Hall measure, *Phys. Rev. E* **102**, 062128 (2020).
- [71] A. S. Holevo, M. Sohma, and O. Hirota, Capacity of quantum gaussian channels, *Phys. Rev. A* **59**, 1820 (1999).
- [72] C. C. Gerry and J. Mimih, Heisenberg-limited interferometry with pair coherent states and parity measurements, *Phys. Rev. A* **82**, 013831 (2010).
- [73] C. C. Gerry and J. Mimih, The parity operator in quantum optical metrology, *Contemp. Phys.* **51**, 497 (2010).
- [74] R. Carranza and C. C. Gerry, Photon-subtracted two-mode squeezed vacuum states and applications to quantum optical interferometry, *J. Opt. Soc. Am. B* **29**, 2581 (2012).
- [75] J. R. Johansson, P. D. Nation, and F. Nori, Qutip: An open-source python framework for the dynamics of open quantum systems, *Comput. Phys. Commun.* **183**, 1760 (2012).
- [76] J. R. Johansson, P. D. Nation, and F. Nori, QuTiP 2: A python framework for the dynamics of open quantum systems, *Comput. Phys. Commun.* **184**, 1234 (2013).
- [77] Y.-S. Ra, A. Dufour, M. Walschaers, C. Jacquard, T. Michel, C. Fabre, and N. Treps, Non-Gaussian quantum states of a multimode light field, *Nat. Phys.* **16**, 144 (2020).
- [78] F. R. Cardoso, D. Z. Rossatto, G. P. L. M. Fernandes, G. Higgins, and C. J. Villas-Boas, Superposition of two-mode squeezed states for quantum information processing and quantum sensing, *Phys. Rev. A* **103**, 062405 (2021).
- [79] M. Walschaers, C. Fabre, V. Parigi, and N. Treps, Statistical signatures of multimode single-photon-added and -subtracted states of light, *Phys. Rev. A* **96**, 053835 (2017).
- [80] M. Walschaers, C. Fabre, V. Parigi, and N. Treps, Entanglement and Wigner Function Negativity of Multimode Non-Gaussian States, *Phys. Rev. Lett.* **119**, 183601 (2017).